

# SCKAN: Structural Consensus-based KAN Prototype Learning for Semi-Supervised Pancreas Segmentation

Yuqi Liu<sup>1</sup>, Yufei Chen<sup>1\*</sup>, Wei Fu<sup>1</sup>, Xiaodong Yue<sup>2</sup>, and Shuo Li<sup>3</sup>

<sup>1</sup> School of Computer Science and Technology, Tongji University, Shanghai, China  
yufeichen@tongji.edu.cn

<sup>2</sup> Artificial Intelligence Institute, Shanghai University, Shanghai, China

<sup>3</sup> Department of Computer and Data Science and Department of Biomedical Engineering, Case Western Reserve University, Cleveland, USA

**Abstract.** Accurate pancreas segmentation is critical for early cancer diagnosis, where annotation scarcity necessitates Semi-Supervised Learning (SSL). However, due to significant inter-sample morphological variability, existing SSL methods face severe generalizability limitations under sparse supervision, leading to the Supervision Bias problem. To address this, we propose **Structural Consensus-based KAN** Prototype Learning (**SCKAN**), which constructs the first cross-sample structural consensus learning with Kolmogorov-Arnold Networks (KANs), to achieve more generalizable and accurate segmentation. Specifically, SCKAN contains two key designs: Structure-constrained Prototype Consistency Learning (SPCL), which prompts unbiased structural representation by enforcing cross-sample consistency via prototype-level contrastive optimization, and Consensus-based Kolmogorov-Arnold Fusion (CKaF), which reduces morphology-specific bias by aggregating stable consensus and filtering sample-wise noise via KAN’s adaptive B-spline nonlinearity. Extensive experiments on two public pancreas datasets demonstrate the effectiveness of SCKAN. Code is at <https://github.com/rhodaliu17/SCKAN>.

**Keywords:** Semi-supervised Learning · Pancreas Segmentation · Kolmogorov-Arnold Network

## 1 Introduction

Accurate pancreas segmentation [1–3] is critical for early cancer diagnosis [4–7], yet scarce annotations make Semi-Supervised Pancreas Segmentation (SSPS) a necessary solution [8–10]. However, due to significant inter-sample morphological variability in the pancreas, existing methods [11–19] suffer from severe generalizability limitations, leading to under- or over-segmentation. Consistency Regularization (CR)-based methods [11–14] enforce sample-wise consistency yet lack

---

\* Corresponding author

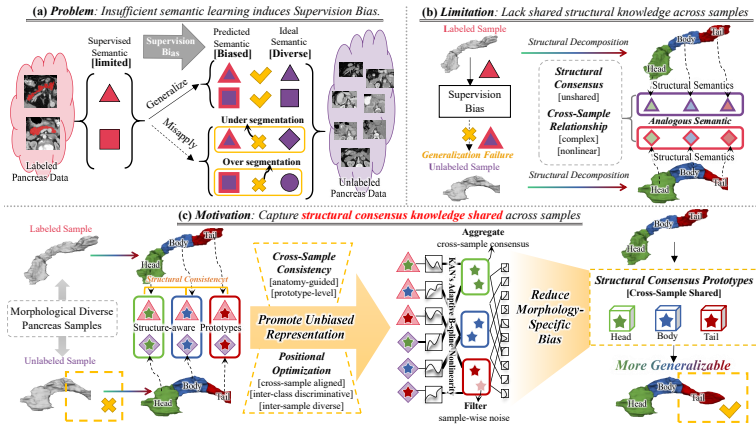


Fig. 1: (a) Limited supervision signals on morphologically diverse pancreas data lead to Supervision Bias. (b) Existing methods suffer from poor generalizability, due to the lack of shared structural knowledge across samples. (c) SCKAN proposes the first cross-sample structural consensus learning with KANs to capture shared knowledge, enhancing generalizability.

effective cross-sample interaction, leaving semantics constrained within supervision. Prototype Learning (PL)-based methods [15–19] capture compact class-wise representations to guide segmentation, but fail to generalize to morphologically diverse samples, with prototype quality constrained by limited supervision.

Insufficient semantic learning constrained by supervision signals induces the *Supervision Bias* problem (Fig. 1(a)). As a result, models fail to generalize beyond labeled guidance, resulting in biased representations. This limitation fundamentally lies in the lack of shared structural knowledge across samples in existing SSPS methods (Fig. 1(b)). Anatomically, the pancreas can be decomposed into head, body, and tail subregions [20, 21], within each of which structural semantics remain analogous across diverse samples, forming the *structural consensus*. However, due to complex and highly nonlinear cross-sample relationships, these structural semantics remain unshared. Kolmogorov-Arnold Networks (KANs) [22], with their superior nonlinear fitting capability, enable effective modeling of such complex cross-sample relationships. Moreover, their adaptive B-spline functions with local support filter morphology-specific noise within local intervals while preserving stable consensus shared across high-variability samples, providing a strong basis for alleviating Supervision Bias.

To address this, we propose **Structural Consensus-based KAN** Prototype Learning (**SCKAN**), the first cross-sample consensus learning with KANs in SSPS (Fig. 1(c)). It captures structural consensus knowledge shared across samples through two key designs: (1) Structure-constrained Prototype Consistency Learning (SPCL), which employs Structure-aware Spatial Decomposition (SSD) to generate anatomy-guided subregion prototypes, establishing cross-sample structural correspondence, and Positional Consistency Calibration (PCC) to adopt

position-weighted contrastive optimization and positional decorrelation regularization, reinforcing cross-sample consistency at the prototype level—thereby promoting unbiased structural representations. (2) Consensus-based Kolmogorov-Arnold Fusion (CKaF), which leverages KAN’s adaptive B-spline nonlinearity to filter sample-wise noise and aggregate stable structural consensus across high-variability samples, thereby reducing morphology-specific bias. **Our contributions are:**

- We first propose structural consensus-based KAN to address supervision bias in SSPS under pancreas morphological diversity.
- Our novel SPCL introduces an anatomy-guided prototype-level consistency mechanism, promoting unbiased structural representation.
- Our novel CKaF introduces a KAN-enhanced cross-sample fusion strategy, aggregating stable consensus and reducing morphology-specific bias.

## 2 Method

SCKAN (Fig. 2) constructs cross-sample structural consensus learning with KANs via two key designs: SPCL (Sec. 2.1) promotes unbiased structural representations via prototype-level cross-sample consistency, and CKaF (Sec. 2.2) reduces morphology-specific bias via KAN-enhanced consensus aggregation. They are jointly optimized via Consensus-Guided Synergetic Learning (Sec. 2.3).

**Preliminaries.** SSPS trains on labeled dataset  $\mathcal{D}_l = \{(X_i^l, Y_i^l)\}_{i=1}^{N_l}$  and unlabeled dataset  $\mathcal{D}_u = \{X_j^u\}_{j=1}^{N_u}$  where  $N_u \gg N_l$ . We adopt the Mean-Teacher framework (Fig. 2(a)), which consists of a student model trained on both datasets, and a teacher model updated via exponential moving average (EMA) of the student’s weights for stable predictions.

### 2.1 SPCL for Promoting Unbiased Structural Representation

SPCL (Fig. 2(b)) employs SSD to enable explicit anatomy-guided cross-sample structural correspondence, and further leverages PCC to reinforce position- and structure-aware cross-sample alignment and intra-sample diversity.

**Structure-aware Spatial Decomposition (SSD)** effectively leverages anatomy-guided K-means clustering on spatial coordinates as a reliable anatomical proxy to decompose features into spatially-coherent ordered subregion prototypes (head, body, tail), grounded in the consistency of relative spatial positions of pancreatic subregions across samples. Given the predicted mask  $\mathbf{M}$  for class  $c$ , we decompose the masked region into  $K$  spatially coherent subregions by applying K-means clustering on the valid spatial coordinates, yielding  $K$  structure-aware regions  $\{\mathbf{R}_k\}_{k=1}^K$ . To ensure consistent cross-sample correspondence, the regions are ordered by their cluster centers  $\{\mathbf{A}_k\}_{k=1}^K$  according to a consistent spatial rule. Given feature map  $\mathbf{F}$  from the 3rd decoder layer (student network  $\mathbf{F}^l$  for labeled data, teacher network  $\mathbf{F}^u$  for unlabeled data), we extract structure-aware prototypes by averaging features  $\mathbf{P}_k = (\sum \mathbf{F} \cdot \mathbf{R}_k) / (\sum \mathbf{R}_k)$ .

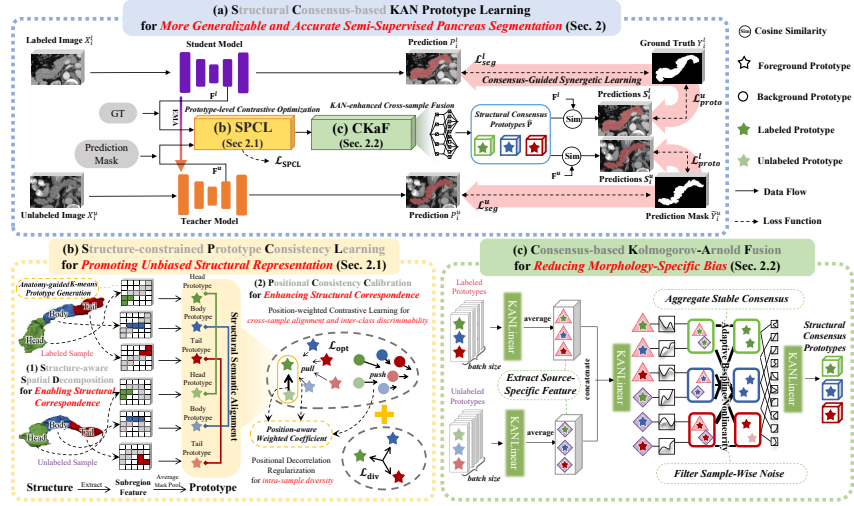


Fig. 2: (a) SCKAN achieves generalizable and accurate SSPS results, consisting of (b) SPCL promoting unbiased structural representation and (c) CKaF reducing morphology-specific bias via aggregating consensus.

**Positional Consistency Calibration (PCC)** novelly calibrates hierarchical semantic relationships among subregion prototypes via position-aware optimization to compact subregion distributions in prototype feature space. It contains two components:

*Position-weighted Contrastive Learning* introduces position-aware weighting to differentiate subregion semantic relationships in contrastive learning, efficiently optimizing cross-sample subregion alignment and inter-class discriminability at the prototype level. For each class  $c$ , let  $\mathbf{P}^l$  and  $\mathbf{P}^u$  denote the prototypes from labeled and unlabeled samples respectively. The complete prototype set is  $\mathbf{P} = \{\mathbf{p}_1^l, \dots, \mathbf{p}_K^l, \bar{\mathbf{p}}^l, \mathbf{p}_1^u, \dots, \mathbf{p}_K^u, \bar{\mathbf{p}}^u\}$ , where  $K$  is the number of subregion prototypes and  $\bar{\mathbf{p}}$  is the average of  $K$  prototypes. We introduce position-aware weighting that assigns different weight coefficients to prototype pairs of each sample:

$$w_{ij} = \begin{cases} 1.0 & \text{if same class and same region} \\ 0.1 & \text{if same class but different region} \end{cases} \quad (1)$$

The position-weighted contrastive optimization loss is formulated as:

$$\mathcal{L}_{\text{opt}} = -\frac{1}{|\mathbf{P}|} \sum_{i \in \mathbf{P}} \log \frac{\mathcal{P}_i^+}{\mathcal{P}_i^+ + \mathcal{P}_i^-}, \quad (2)$$

where  $\mathcal{P}_i^+$  and  $\mathcal{P}_i^-$  are defined as  $\mathcal{P}_i^+ = \sum_{j \in \mathbf{P}_i^+} w_{ij} \cdot \exp(\text{sim}(\mathbf{P}_i, \mathbf{P}_j)/\tau)$  and  $\mathcal{P}_i^- = \sum_{j \in \mathbf{P}_i^-} \exp(\text{sim}(\mathbf{P}_i, \mathbf{P}_j)/\tau)$ .  $\mathbf{P}_i^+$  denotes positive pairs (same class as pro-

totype  $i$ ),  $\mathcal{P}_i^-$  denotes negative pairs (different class),  $\text{sim}(\cdot, \cdot)$  is cosine similarity, and  $\tau$  is the temperature parameter.

*Positional Decorrelation Regularization* imposes a position-sensitive similarity penalty on intra-sample structure-aware prototypes to ensure subregion diversity and distinct characteristics via:

$$\mathcal{L}_{\text{div}} = \frac{1}{|\mathcal{C}|} \sum_{c \in \mathcal{C}} \frac{1}{K(K-1)} \sum_{k \neq k'} \max(0, \text{sim}(\mathbf{P}_k^c, \mathbf{P}_{k'}^c) - \alpha), \quad (3)$$

where  $\mathcal{C}$  is the total class number and the threshold  $\alpha$  encourages moderate diversity.

With  $\lambda_{\text{div}}$  balancing their contributions, the SPCL loss is formulated as:

$$\mathcal{L}_{\text{SPCL}} = (1 - \lambda_{\text{div}})\mathcal{L}_{\text{opt}} + \lambda_{\text{div}}\mathcal{L}_{\text{div}}. \quad (4)$$

**Summary of Advantage:** SPCL novelly designs anatomy-guided K-means prototype generation in SSD, position-weighted contrastive optimization and positional similarity penalty in PCC, promoting unbiased structural representations.

## 2.2 CKaF for Reducing Morphology-Specific Bias

CKaF (Fig. 2(c)) filters sample-wise noise and aggregates stable structural consensus across diverse samples through KAN-enhanced cross-sample fusion, leveraging adaptive B-spline functions with local support to reduce morphology-specific bias and greatly improve generalizability. Given structure-aware prototypes  $\mathbf{P}^l$  and  $\mathbf{P}^u$  from labeled and unlabeled samples, we apply separate KAN fusion to extract source-specific features:

$$\mathbf{H}^l = \text{KANLinear}_l(\mathbf{P}^l), \quad \mathbf{H}^u = \text{KANLinear}_u(\mathbf{P}^u), \quad (5)$$

where  $\text{KANLinear}(\mathbf{x}) = \sum_i h_i(x_i)$  is the KAN layer with learnable B-spline functions  $h(\cdot)$  [22]. Batch-level average pooling retains statistically stable structural knowledge across diverse samples, and the resulting representations are then integrated through two-stage KAN fusion to synthesize cross-sample structural consensus prototype  $\hat{\mathbf{P}}$ , where  $\oplus$  is concatenation and  $B$  is batch size:

$$\mathbf{H} = \text{KANLinear} \left( \left[ \frac{1}{B^l} \sum_{n=1}^{B^l} \mathbf{H}_n^l \oplus \frac{1}{B^u} \sum_{m=1}^{B^u} \mathbf{H}_m^u \right] \right), \quad \hat{\mathbf{P}} = \text{KANLinear}(\mathbf{H}). \quad (6)$$

This hierarchical design utilizes KAN’s superior fitting capacity to effectively model complex and nonlinear cross-sample relationships, efficiently aggregating cross-sample structural consensus knowledge.

**Summary of Advantage:** CKaF aggregates stable consensus by designing KAN-enhanced cross-sample fusion strategy for reducing morphology-specific bias.

Table 1: Comparison of different methods on NIH-PAN and MSD-PAN datasets demonstrating the advantages of our method. Results are reported as mean $\pm$ std. Best results are in **red**, second-best in **blue**.

NIH-PAN Dataset												
Method	Type	Lb/ULb	Dice $\uparrow$	Jaccard $\uparrow$	HD95 $\downarrow$	ASD $\downarrow$		Lb/ULb	Dice $\uparrow$	Jaccard $\uparrow$	HD95 $\downarrow$	ASD $\downarrow$
V-NET	SL	62/0 (100%)	83.11 $\pm$ 5.57	71.46 $\pm$ 7.85	5.16 $\pm$ 3.76	1.05 $\pm$ 0.23		-	-	-	-	-
V-NET	SL	3/0 (5%)	24.64 $\pm$ 21.18	15.84 $\pm$ 14.91	42.74 $\pm$ 42.43	7.00 $\pm$ 6.22		6/0 (10%)	53.76 $\pm$ 17.02	38.58 $\pm$ 15.79	20.35 $\pm$ 14.62	3.17 $\pm$ 5.20
UA-MT	SSL		35.71 $\pm$ 12.21	22.41 $\pm$ 9.08	57.97 $\pm$ 13.81	25.12 $\pm$ 7.22			67.66 $\pm$ 14.73	52.78 $\pm$ 14.91	14.64 $\pm$ 11.90	2.84 $\pm$ 1.97
SASSNet	SSL		50.87 $\pm$ 13.92	35.28 $\pm$ 12.65	30.23 $\pm$ 13.67	10.71 $\pm$ 6.26			70.96 $\pm$ 15.44	56.82 $\pm$ 15.37	12.10 $\pm$ 1.15	4.69 $\pm$ 6.59
URPC	SSL		49.68 $\pm$ 17.89	34.76 $\pm$ 14.55	26.44 $\pm$ 13.19	6.36 $\pm$ 3.77			73.66 $\pm$ 11.95	59.45 $\pm$ 12.33	12.00 $\pm$ 8.08	2.34 $\pm$ 1.02
BCP	SSL		<b>74.90<math>\pm</math>7.39</b>	<b>60.39<math>\pm</math>8.91</b>	11.38 $\pm$ 11.96	2.00 $\pm$ 1.04			<b>82.59<math>\pm</math>4.36</b>	<b>70.57<math>\pm</math>6.10</b>	6.10 $\pm$ 4.05	1.73 $\pm$ 1.06
AD-MT	SSL	3/59 (5%)	67.46 $\pm$ 5.48	51.15 $\pm$ 6.07	13.70 $\pm$ 6.91	1.93 $\pm$ 0.60		6/56 (10%)	80.73 $\pm$ 6.52	68.18 $\pm$ 8.77	7.03 $\pm$ 6.66	1.39 $\pm$ 0.58
CPCL	PL-SSL		50.88 $\pm$ 21.96	36.72 $\pm$ 17.84	33.16 $\pm$ 23.76	10.19 $\pm$ 14.51			69.09 $\pm$ 13.89	54.23 $\pm$ 14.60	17.19 $\pm$ 15.45	3.69 $\pm$ 3.76
UPCoL	PL-SSL		51.77 $\pm$ 18.84	36.86 $\pm$ 15.41	32.90 $\pm$ 24.42	3.32 $\pm$ 3.03			72.78 $\pm$ 13.41	58.72 $\pm$ 14.45	14.00 $\pm$ 15.52	4.07 $\pm$ 3.87
BaPC	PL-SSL		41.59 $\pm$ 18.19	27.88 $\pm$ 14.30	51.30 $\pm$ 30.85	3.86 $\pm$ 5.58			75.10 $\pm$ 11.18	61.24 $\pm$ 12.50	12.26 $\pm$ 15.82	3.26 $\pm$ 4.49
MPER	PL-SSL		74.88 $\pm$ 6.39	60.24 $\pm$ 7.67	<b>9.15<math>\pm</math>3.84</b>	<b>2.34<math>\pm</math>1.08</b>			82.76 $\pm$ 4.88	70.87 $\pm$ 6.70	<b>5.32<math>\pm</math>2.35</b>	<b>1.55<math>\pm</math>0.71</b>
SCKAN	PL-SSL		<b>78.91<math>\pm</math>4.17</b>	<b>65.36<math>\pm</math>5.62</b>	<b>6.67<math>\pm</math>2.90</b>	<b>1.80<math>\pm</math>0.66</b>			<b>83.91<math>\pm</math>3.82</b>	<b>72.47<math>\pm</math>5.55</b>	<b>4.61<math>\pm</math>1.82</b>	<b>1.33<math>\pm</math>0.56</b>
MSD-PAN Dataset												
Method	Type	Lb/ULb	Dice $\uparrow$	Jaccard $\uparrow$	HD95 $\downarrow$	ASD $\downarrow$		Lb/ULb	Dice $\uparrow$	Jaccard $\uparrow$	HD95 $\downarrow$	ASD $\downarrow$
V-NET	SL	168/0 (100%)	67.20 $\pm$ 19.79	53.40 $\pm$ 19.01	12.32 $\pm$ 17.36	2.31 $\pm$ 3.40		-	-	-	-	-
V-NET	SL	17/0 (10%)	32.42 $\pm$ 30.18	23.61 $\pm$ 23.83	30.55 $\pm$ 32.77	6.34 $\pm$ 8.64		34/0 (20%)	56.51 $\pm$ 21.50	42.28 $\pm$ 19.55	20.29 $\pm$ 18.89	4.57 $\pm$ 4.56
UA-MT	SSL		40.15 $\pm$ 26.01	28.55 $\pm$ 21.20	33.53 $\pm$ 16.67	12.72 $\pm$ 8.85			55.62 $\pm$ 23.37	41.88 $\pm$ 20.90	29.30 $\pm$ 31.19	2.25 $\pm$ 1.80
SASSNet	SSL		39.56 $\pm$ 23.42	27.38 $\pm$ 18.80	35.00 $\pm$ 17.39	14.40 $\pm$ 9.03			57.79 $\pm$ 19.55	43.13 $\pm$ 18.32	20.22 $\pm$ 17.60	4.61 $\pm$ 3.40
URPC	SSL		43.02 $\pm$ 26.67	31.14 $\pm$ 22.23	32.20 $\pm$ 19.53	6.10 $\pm$ 5.06			59.08 $\pm$ 19.54	44.52 $\pm$ 18.85	20.56 $\pm$ 17.32	4.18 $\pm$ 4.31
BCP	SSL		57.63 $\pm$ 18.02	42.67 $\pm$ 17.48	21.58 $\pm$ 13.26	7.05 $\pm$ 4.45			<b>62.63<math>\pm</math>17.53</b>	47.77 $\pm$ 17.27	<b>19.72<math>\pm</math>25.49</b>	<b>2.04<math>\pm</math>1.44</b>
AD-MT	SSL	17/134 (10%)	<b>59.74<math>\pm</math>21.58</b>	<b>45.57<math>\pm</math>19.60</b>	20.86 $\pm$ 26.00	<b>3.22<math>\pm</math>4.33</b>		34/134 (20%)	62.14 $\pm$ 23.61	<b>48.67<math>\pm</math>21.27</b>	22.96 $\pm$ 31.38	2.66 $\pm$ 4.16
CPCL	PL-SSL		29.95 $\pm$ 30.39	21.86 $\pm$ 23.90	40.57 $\pm$ 40.89	6.19 $\pm$ 9.77			50.64 $\pm$ 26.84	38.00 $\pm$ 23.01	36.38 $\pm$ 36.32	2.84 $\pm$ 3.84
UPCoL	PL-SSL		43.35 $\pm$ 30.51	32.46 $\pm$ 24.78	41.42 $\pm$ 37.80	8.79 $\pm$ 11.55			59.56 $\pm$ 21.21	45.34 $\pm$ 19.61	25.92 $\pm$ 29.53	2.78 $\pm$ 4.20
BaPC	PL-SSL		42.93 $\pm$ 30.06	32.04 $\pm$ 24.83	44.00 $\pm$ 40.07	6.93 $\pm$ 11.43			56.15 $\pm$ 25.33	42.85 $\pm$ 21.91	32.83 $\pm$ 34.81	3.30 $\pm$ 5.24
MPER	PL-SSL		55.65 $\pm$ 18.99	40.90 $\pm$ 18.03	<b>19.97<math>\pm</math>13.08</b>	6.71 $\pm$ 4.68			59.43 $\pm$ 18.42	44.54 $\pm$ 17.37	23.27 $\pm$ 27.97	3.24 $\pm$ 2.60
SCKAN	PL-SSL		<b>61.71<math>\pm</math>18.00</b>	<b>46.94<math>\pm</math>17.97</b>	<b>19.35<math>\pm</math>23.70</b>	<b>4.07<math>\pm</math>4.05</b>			<b>63.72<math>\pm</math>17.50</b>	<b>48.97<math>\pm</math>17.47</b>	<b>17.66<math>\pm</math>22.33</b>	<b>2.03<math>\pm</math>1.09</b>

### 2.3 Consensus-Guided Synergetic Learning for Segmentation

Structural consensus knowledge is bridged between the prototype space and the segmentation network via consistency regularization, enabling the two branches to synergistically learn from each other (Fig. 2(a)). We define the hybrid loss as  $\mathcal{L}_{\text{hybrid}} = \frac{1}{2}(\mathcal{L}_{\text{Dice}} + \mathcal{L}_{\text{CE}})$ . For the segmentation network, we apply supervised loss on labeled data  $\mathcal{L}_{\text{seg}}^l = \mathcal{L}_{\text{hybrid}}(P^l, Y^l)$  and consistency regularization on unlabeled data with pseudo-labels  $\tilde{Y}^u$  from the teacher model  $\mathcal{L}_{\text{seg}}^u = \mathcal{L}_{\text{hybrid}}(P^u, \tilde{Y}^u)$ . We then enforce consistency between segmentation network and prototype-based predictions  $S = \arg \max_c \max_k \text{sim}(\mathbf{F}, \hat{\mathbf{P}}_k^c)$ . We apply the same hybrid loss to the prototype-based predictions with  $\mathcal{L}_{\text{proto}}^l = \mathcal{L}_{\text{hybrid}}(S^l, Y^l)$  and  $\mathcal{L}_{\text{proto}}^u = \mathcal{L}_{\text{hybrid}}(S^u, \tilde{Y}^u)$ . The final training objective combines all components:

$$\mathcal{L}_{\text{total}} = \mathcal{L}_{\text{seg}}^l + \mathcal{L}_{\text{seg}}^u + \mathcal{L}_{\text{proto}}^l + \lambda_{\text{gs}}(\mathcal{L}_{\text{proto}}^u + \mathcal{L}_{\text{SPCL}}), \quad (7)$$

where  $\lambda_{\text{gs}} = e^{-5(1-s/s_{\text{max}})^2}$  is a time-dependent Gaussian warming-up function [23] that gradually increases consensus learning contribution during training.

## 3 Experiments

### 3.1 Experimental Setup

**Datasets.** We evaluate on two pancreas datasets. **(a)** *NIH-PAN* [24] contains 80 contrast-enhanced CT scans, with 62 for training and 18 for testing. **(b)** *MSD-*

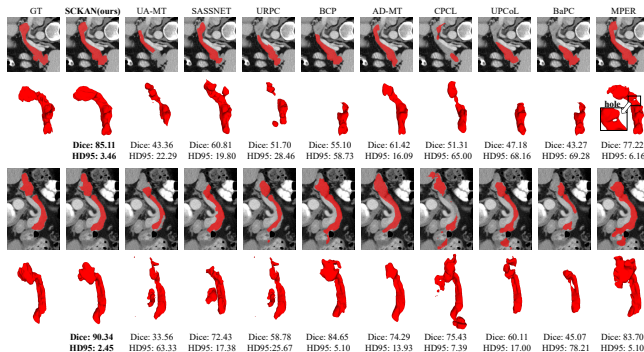


Fig. 3: 2D slice, 3D visualizations and metric performance on 5% NIH-PAN dataset illustrating our method’s capability in preserving structural completeness and achieving accurate segmentation without extra predictions.

PAN [25] contains 281 annotated cases, where pancreas and tumor labels are merged into a single foreground class following [26, 27], with 168 for training, 57 for validation, and 56 for testing. **Implementation Details.** SCKAN is implemented in PyTorch and trained on a single NVIDIA RTX 3090 GPU. V-Net serves as the backbone of all methods. We use a batch size of 8 with 4 labeled and 4 unlabeled data, SGD optimizer with momentum 0.9, initial learning rate 0.01, and EMA decay 0.99. Data augmentation includes random cropping and copy-paste [28, 29]. Prototype number is set to  $K = 3$  to correspond to structural decomposition for head, body and tail. Images are resized to  $96 \times 96 \times 96$  following [12, 15]. Performance is measured via Dice, Jaccard, HD95, and ASD.

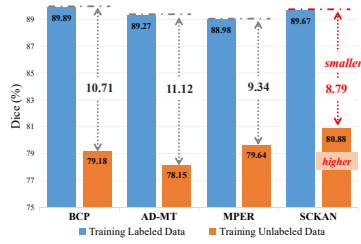
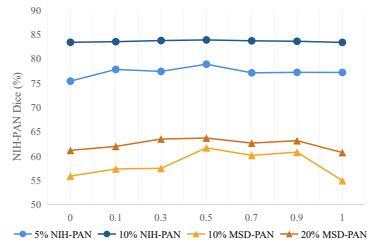
### 3.2 Results and Analysis

**Comparison with State-of-the-Arts (Table 1, Fig. 3, Fig. 4).** Experiments are conducted on two pancreas datasets to demonstrate our advantage. Our method achieves superior metrics, particularly under extreme supervision scarcity (5% NIH-PAN, only 3 samples), demonstrating enhanced structural completeness and accurate segmentation. On the more challenging MSD-PAN with lower image quality, our method still achieves competitive results with consistently low variance. Visualizations in Fig. 3 further validate our advantage with substantially higher Dice and lower HD95. Fig. 4 reveals that our method effectively alleviates Supervision Bias, yielding more generalizable results.

**Ablation on Key Components (Table 2).** We validate each component on 10% NIH-PAN. The baseline Mean Teacher (MT) with prototype learning (PL) achieves 77.69% Dice, confirming the benefit of prototype-enhanced consistency regularization. Introducing SSD further improves Dice to 80.21% and SSD+PCC contributes an additional +2.4% Dice, validating the advantage of prompting unbiased structural representations in SPCL. CKaF alone yields 81.92%, confirming effective cross-sample consensus aggregation. The full

Table 2: Ablation study on key components under 10% NIH-PAN validating the effectiveness of our novel designs. Improvements are relative to MT+PL.

MT	PL	SPCL		CKaF	Dice $\uparrow$	Jaccard $\uparrow$	HD95 $\downarrow$	ASD $\downarrow$
		SSD	PCC					
$\checkmark$					66.60	52.55	18.97	6.12
$\checkmark$	$\checkmark$				77.69	64.16	9.15	2.09
$\checkmark$	$\checkmark$	$\checkmark$			80.21 ( $\uparrow 2.52$ )	67.36 ( $\uparrow 3.20$ )	5.92 ( $\downarrow 3.23$ )	1.62 ( $\downarrow 0.47$ )
$\checkmark$	$\checkmark$	$\checkmark$	$\checkmark$		82.61 ( $\uparrow 4.92$ )	70.59 ( $\uparrow 6.43$ )	5.42 ( $\downarrow 3.73$ )	1.57 ( $\downarrow 0.52$ )
$\checkmark$	$\checkmark$			$\checkmark$	81.92 ( $\uparrow 4.23$ )	69.63 ( $\uparrow 5.47$ )	5.91 ( $\downarrow 3.24$ )	1.68 ( $\downarrow 0.41$ )
$\checkmark$	$\checkmark$	$\checkmark$	$\checkmark$	$\checkmark$	<b>83.91 (<math>\uparrow 6.22</math>)</b>	<b>72.47 (<math>\uparrow 8.31</math>)</b>	<b>4.61 (<math>\downarrow 4.54</math>)</b>	<b>1.33 (<math>\downarrow 0.76</math>)</b>

Fig. 4: Comparison of methods (only Dice gap  $< 20\%$ ) between labeled and unlabeled data on 10% NIH-PAN.Fig. 5: Ablation study on diversity loss coefficient  $\lambda_{\text{div}}$  on both datasets. Best results at 0.5.

SCKAN achieves optimal performance, with SPCL and CKaF synergistically contributing to accurate segmentation.

**Ablation on Diversity Loss Coefficient  $\lambda_{\text{div}}$  (Fig. 5).** The coefficient  $\lambda_{\text{div}}$  balances  $\mathcal{L}_{\text{opt}}$  and  $\mathcal{L}_{\text{div}}$  in SPCL, controlling the trade-off between cross-sample structural correspondence and intra-sample diversity. Setting  $\lambda_{\text{div}} = 0$  causes prototypes to collapse into overly similar representations, while  $\lambda_{\text{div}} = 1.0$  sacrifices inter-sample alignment. Performance remains stable across intermediate values, with the best results achieved at  $\lambda_{\text{div}} = 0.5$ , reaching optimal balance.

**Ablation on Fusion Strategies (Table 3).** We compare three prototype fusion strategies to validate the effectiveness of our **KAN-enhanced cross-sample fusion** strategy in alleviating Supervision Bias. Our fusion achieves the best overall performance on both datasets. Compared with the competitive Multi-layer Perceptron (MLP) fusion strategy, we further narrow the L-U Dice gap by 6.84% and 2.52% on two datasets, respectively. This demonstrates that our CKaF better reduces morphology-specific bias by filtering sample-wise noise and aggregating cross-sample consensus.

## 4 Conclusion

SCKAN addresses the Supervision Bias problem in SSPS under pancreatic diversity by constructing the first structural consensus-based KAN. Building on this, SPCL enforces cross-sample consistency via prototype-level contrastive op-

Table 3: Ablation study on three prototype fusion strategies showing the effectiveness of KAN-enhanced cross-sample fusion in alleviating Supervision Bias.

Fusion strategy	5% NIH-PAN				10% MSD-PAN			
	Dice $\uparrow$	L-Dice	U-Dice	L-U Dice $\downarrow$	Dice $\uparrow$	L-Dice	U-Dice	L-U Dice $\downarrow$
Average Fusion	75.96	87.97	71.56	16.38	59.30	92.75	69.97	22.78
MLP Fusion	77.45	90.10	74.61	15.49	60.94	92.25	70.82	21.43
<b>KAN Fusion (ours)</b>	<b>78.91</b>	89.96	81.31	<b>8.65</b> ( <b><math>\downarrow</math>6.84</b> )	<b>61.71</b>	89.79	70.88	<b>18.91</b> ( <b><math>\downarrow</math>2.52</b> )

\*‘L’ and ‘U’ denote training labeled and unlabeled data, respectively. ‘L-U Dice’ means their Dice gap.

timization for unbiased structural representations, and CKaF aggregates stable cross-sample consensus via KAN’s adaptive B-spline nonlinearity to reduce morphology-specific bias. Extensive experiments validate the effectiveness and generalizability of SCKAN. Code is available at <https://github.com/rhodaliu17/SCKAN>.

**Acknowledgments.** This work was supported by the National Natural Science Foundation of China (No. 62472315, No. 62476165).

**Disclosure of Interests.** The authors have no competing interests to declare that are relevant to the content of this article.

## References

1. Andrea Moglia, Matteo Cavicchioli, Luca Mainardi, and Pietro Cerveri. Deep learning for pancreas segmentation on computed tomography: a systematic review. *Artificial Intelligence Review*, 58(8), 2025.
2. Yufei Chen, Chang Xu, Weiping Ding, Shichen Sun, Xiaodong Yue, and Hamido Fujita. Target-aware u-net with fuzzy skip connections for refined pancreas segmentation. *Applied Soft Computing*, 131:109818, 2022.
3. Zheyuan Zhang, Lanhong Yao, Elif Keles, Yury Velichko, and Ulas Bagci. Deep learning algorithms for pancreas segmentation from radiology scans: A review. *Advances in Clinical Radiology*, 5(1):31–52, 2023.
4. Christopher J Halbrook, Costas A Lyssiotis, Marina Pasca di Magliano, and Anirban Maitra. Pancreatic cancer: advances and challenges. *Cell*, 186(8):1729–1754, 2023.
5. Elena M Stoffel, Randall E Brand, and Michael Goggins. Pancreatic cancer: changing epidemiology and new approaches to risk assessment, early detection, and prevention. *Gastroenterology*, 164(5):752–765, 2023.
6. Wei Fu, Yufei Chen, Yuqi Liu, and Xiaodong Yue. D-edl: Differential evidential deep learning for robust medical out-of-distribution detection. *Medical Image Analysis*, page 103888, 2025.
7. Wei Fu, Yufei Chen, Wei Liu, Xiaodong Yue, and Chao Ma. Evidence reconciled neural network for out-of-distribution detection in medical images. In *International Conference on Medical Image Computing and Computer-Assisted Intervention*, pages 305–315. Springer, 2023.
8. Ziman Yin, Dong Nie, Shuo Li, Junjun Pan, and Zhenyu Tang. Iterative foundation-dedicated learning: Optimized key frames, prompts and memories for

- semi-supervised segmentation. In *International Conference on Medical Image Computing and Computer-Assisted Intervention*, pages 258–267. Springer, 2025.
9. Tao Wang, Xinlin Zhang, Yuanbin Chen, Yuanbo Zhou, Longxuan Zhao, Tao Tan, and Tong Tong. Synergy-guided regional supervision of pseudo labels for semi-supervised medical image segmentation. In *International Conference on Medical Image Computing and Computer-Assisted Intervention*, pages 530–540. Springer, 2025.
  10. Zhen Zhao, Zicheng Wang, Longyue Wang, Dian Yu, Yixuan Yuan, and Luping Zhou. Alternate diverse teaching for semi-supervised medical image segmentation. In *European Conference on Computer Vision*, pages 227–243. Springer, 2024.
  11. Lequan Yu, Shujun Wang, Xiaomeng Li, Chi-Wing Fu, and Pheng-Ann Heng. Uncertainty-aware self-ensembling model for semi-supervised 3d left atrium segmentation. In *Medical image computing and computer assisted intervention—MICCAI 2019: 22nd international conference, Shenzhen, China, October 13–17, 2019, proceedings, part II 22*, pages 605–613. Springer, 2019.
  12. Xiangde Luo, Guotai Wang, Wenjun Liao, Jieneng Chen, Tao Song, Yinan Chen, Shichuan Zhang, Dimitris N Metaxas, and Shaoting Zhang. Semi-supervised medical image segmentation via uncertainty rectified pyramid consistency. *Medical Image Analysis*, 80:102517, 2022.
  13. Xiangde Luo, Jieneng Chen, Tao Song, and Guotai Wang. Semi-supervised medical image segmentation through dual-task consistency. In *Proceedings of the AAAI conference on artificial intelligence*, volume 35, pages 8801–8809, 2021.
  14. Yantao Chen, Yong Ma, Xiaoguang Mei, Lin Zhang, Zhigang Fu, and Jiayi Ma. Triple-task mutual consistency for semi-supervised 3d medical image segmentation. *Computers in Biology and Medicine*, 175:108506, 2024.
  15. Wenjing Lu, Jiahao Lei, Peng Qiu, Rui Sheng, Jinhua Zhou, Xinwu Lu, and Yang Yang. Upcol: uncertainty-informed prototype consistency learning for semi-supervised medical image segmentation. In *International Conference on Medical Image Computing and Computer-Assisted Intervention*, pages 662–672. Springer, 2023.
  16. Zhe Xu, Yixin Wang, Donghuan Lu, Lequan Yu, Jiangpeng Yan, Jie Luo, Kai Ma, Yefeng Zheng, and Raymond Kai-yu Tong. All-around real label supervision: Cyclic prototype consistency learning for semi-supervised medical image segmentation. *IEEE Journal of Biomedical and Health Informatics*, 26(7):3174–3184, 2022.
  17. Yali Bi, Enyu Che, Yinan Chen, Yuanpeng He, and Jingwei Qu. Multi-prototype-based embedding refinement for medical image segmentation. In *ICASSP 2025 - 2025 IEEE International Conference on Acoustics, Speech and Signal Processing (ICASSP)*, pages 1–5, 2025.
  18. Yongchao Wang, Bin Xiao, Xiuli Bi, Weisheng Li, and Xinbo Gao. Boundary-aware prototype in semi-supervised medical image segmentation. *IEEE Transactions on Image Processing*, 2024.
  19. Yuqi Liu, Yufei Chen, Wei Fu, Xiaodong Yue, and Thierry Deneux. Kp2l: Knowledge-driven pyramid prototype learning for semi-supervised medical image segmentation. *Knowledge-Based Systems*, 340:115662, 2026.
  20. Sehrish Javed, Touseef Ahmad Qureshi, Zengtian Deng, Ashley Wachsman, Yaniv Raphael, Srinivas Gaddam, Yibin Xie, Stephen Jacob Pandol, and Debiao Li. Segmentation of pancreatic subregions in computed tomography images. *Journal of Imaging*, 8(7):195, 2022.
  21. Sehrish Javed, Touseef Ahmad Qureshi, Srinivas Gaddam, Lixia Wang, Linda Azab, Ashley Max Wachsman, Wansu Chen, Vahid Asadpour, Christie Younghae

- Jeon, Beichien Wu, et al. Risk prediction of pancreatic cancer using ai analysis of pancreatic subregions in computed tomography images. *Frontiers in oncology*, 12:1007990, 2022.
22. Ziming Liu, Yixuan Wang, Sachin Vaidya, Fabian Ruehle, James Halverson, Marin Soljagic, Thomas Y Hou, and Max Tegmark. Kan: Kolmogorov–arnold networks. In *The Thirteenth International Conference on Learning Representations*, 2025.
  23. Samuli Laine and Timo Aila. Temporal ensembling for semi-supervised learning. In *International Conference on Learning Representations*, 2017.
  24. Holger R Roth, Amal Farag, E Turkbey, Le Lu, Jiamin Liu, and Ronald M Summers. Data from pancreas-ct. the cancer imaging archive. *IEEE Transactions on Image Processing*, 5, 2016.
  25. Michela Antonelli, Annika Reinke, Spyridon Bakas, et al. The medical segmentation decathlon. *Nature Communications*, 2022.
  26. Yue Zhang, Jiong Wu, Yilong Liu, Yifan Chen, Wei Chen, Ed X Wu, Chunming Li, and Xiaoying Tang. A deep learning framework for pancreas segmentation with multi-atlas registration and 3d level-set. *Medical Image Analysis*, 68:101884, 2021.
  27. Yue Gou, Yuming Xing, Shengzhu Shi, and Zhichang Guo. Diffusion probabilistic multi-cue level set for reducing edge uncertainty in pancreas segmentation. *Biomedical Signal Processing and Control*, 106:107744, 2025.
  28. Yunhao Bai, Duowen Chen, Qingli Li, Wei Shen, and Yan Wang. Bidirectional copy-paste for semi-supervised medical image segmentation. In *Proceedings of the IEEE/CVF conference on computer vision and pattern recognition*, pages 11514–11524, 2023.
  29. Sangdoo Yun, Dongyoon Han, Sanghyuk Chun, Seong Joon Oh, Youngjoon Yoo, and Junsuk Choe. Cutmix: Regularization strategy to train strong classifiers with localizable features. In *2019 IEEE/CVF International Conference on Computer Vision (ICCV)*, pages 6022–6031, 2019.